N-O-D-15-00671R3

1 **Glioblastoma on a microfluidic chip: Generating pseudopalisades and enhancing**

2 **aggressiveness through blood vessel obstruction events**

3 Jose M. Ayuso[123], Rosa Monge[123], Alicia Martínez-González[4], María Virumbrales-

4 Muñoz[123], Guillermo A. Llamazares[123], Javier Berganzo[5], Aurelio Hernández-Laín[6],

5 Jorge Santolaria[7], Manuel Doblaré[123], Christopher Hubert[8], Jeremy N. Rich[8], Pilar

6 Sánchez-Gómez[9], Víctor M. Pérez-García[4], Ignacio Ochoa[123*], Luis J. Fernández[123*].

7 1 Group of Structural Mechanics and Materials Modelling (GEMM). Centro Investigación Biomédica en Red.

8 Bioingenieria, biomateriales y nanomedicina (CIBER-BBN), Spain.

9 2 Aragón Institute of Engineering Research (I3A), University of Zaragoza, Spain.

10 3 Aragon Institute of Biomedical Research, Instituto de Salud Carlos III, Spain.

11 4 Institute of Applied Mathematics in Science and Engineering, Castilla-La Mancha University, Spain.

12 5 MEMS/MST Department, Ikerlan S. Coop., Mondragón, Spain.

13 6 Department of Pathology (Neuropathology), Hospital Universitario 12 de Octubre Research Institute, Madrid, Spain.

14 7 Department of Design and Manufacturing Engineering, University of Zaragoza, Spain.

15 8 Department of Stem Cell Biology and Regenerative Medicine, Lerner Research Institute, Cleveland Clinic, Cleveland,

16 OH 44195

17 9 Neuro-oncology unit. Health institute Carlos III-UFIEC, Spain.

18 * These authors equally coordinate this project.

19 Running title: Glioblastoma pseudopalisades on a chip

20 Corresponding author: Luis José Fernández. Mailing address: Mariano Esquillor, Zaragoza,

21 Zaragoza, Spain, 50018. Phone: 876555467. Fax: 976762043. E-Mail: luisf@unizar.es

30 Conflict of interests: All the authors declare no competing interests.

31   Word   count: 6433

32

ABSTRACT

34

Background: Glioblastoma (GBM) is one of the most lethal tumor types. Hypercellular regions, named pseudopalisades, are characteristic in these tumors and have been hypothesized to be waves of migrating glioblastoma cells. These "waves" of cells are thought to be induced by oxygen and nutrient depletion caused by tumor-induced blood vessel occlusion. Although the universal presence of these structures in GBM tumors suggest that they may play an instrumental role in GBM spreading and invasion, the recreation of these structures in vitro has remained challenging.

Methods: Here we present a new microfluidic model of GBM that mimics the dynamics of pseudopalisade formation. To do this, we embedded U-251 MG cells within a collagen hydrogel in a custom designed microfluidic device. By controlling the medium flow through lateral microchannels, we can mimic and control blood vessel obstruction events associated with this disease.

Results: Through the use of this new system, we show that nutrient and oxygen starvation triggers a strong migratory process leading to pseudopalisade generation in vitro. These results validate the hypothesis of pseudopalisade formation and show an excellent agreement with a systems-biology model based on hypoxia-driven phenomenon.

Conclusions: This paper shows the potential of microfluidic devices as advanced artificial systems capable of modeling in vivo nutrient and oxygen gradients during tumor evolution.

Keywords: Glioblastoma, Microfluidics, Pseudopalisades, SU-8, Migration

56

57

58

59

60   **INTRODUCTION**

61

62   Glioblastoma, also named grade IV astrocytoma, is the most common and lethal

63   malignant primary brain tumor. Patients receiving the standard-of-care based on local

64   radiotherapy and concomitant chemotherapy have a median survival of 14 months[1].

65   Despite the efforts of the research community, new treatments to tackle the disease

66   are still far from the clinic. GBM tumors are highly infiltrating and fast progressing

67   tumors[2] and are characterized by two main histopathological conditions: necrotic foci

68   typically surrounded by areas of high cellularity known as pseudopalisading regions,

69   and microvascular proliferation[2].

70

71   The causes of these densely populated pesudopalisades remain poorly understood.

72   Although the high cellularity was initially thought to be due to rapid proliferation of GBM

73   cells, recent histological studies have shown that proliferation in pseudopalisading

74   areas is significantly lower than in adjacent regions[3]. Additionally, in pseudopalisades

75   apoptosis is substantially larger than in neighboring regions[4]. This evidence suggests

76   that pseudopalisades are due to causes other than simply higher proliferation or

77   survival rates. Recent reports have shown that in histological slices from GBM patients

78   more than 50% of pseudopalisades clearly present a central obstructed blood vessel,

79   and microscopic evidence of thrombosis is observed in more than 90% of samples[4-6].

80

81   GBM cells express several procoagulant factors which may serve to induce

82   thrombosis[7]. Additional evidence shows that cells in pseudopalisades are hypoxic and

83   overexpress HIF-1α[8]. Although this hypoxic microenvironment leads to microvascular

84   hyperplasia, the associated microcirculation is very inefficient due to parenchymal

85   edema and poor maintenance of the blood brain barrier[9]. As a consequence, the

86   supply of oxygen and nutrients is compromised in the zone surrounding a thrombosis.

87   GBM evolution is a complex process. It has been proposed that one of the driving

88   forces of glioma aggressiveness is nutrient and oxygen starvation[3,4,10]. First, GBM

89   proliferation and secretion of pro-coagulant signals would causes thrombotic events

90   leading to hypoxia and nutrient depletion. As a consequence, the migration of cells

91   away from a thrombosis and towards nutrients and oxygen enriched regions could

92   create the characteristic GBM pseudopalisades. Eventually, these migrating cells

93   would reach other blood vessels and eventually cause the collapse of these vessels,

94   restarting the process and creating another expanding wave of tumor cells within the

95   brain. This hypothesis proposes that GBM cells are exposed to cyclic starvation which

96   forces their metabolism to switch between a proliferative or migrating phenotype.

97

98   Since we cannot take multiple histologic timepoints in vivo, it has not been possible to

99   definitively observe thrombosis-induced migration in real-time and the kinetics of any

100   such migration are not understood. This complex process is not reproducible using

101   standard "in vitro" models because the conventional migration assays are unable to

102   mimic the complex microenvironment described. Recently, microfabrication and

103   microfluidic technologies have arisen, allowing the design and creation of custom high-

104   performance cell culture systems[11]. In this paper we describe the design, fabrication

105   and biological validation of a microfluidic device using SU-8 technology for three-

106   dimensional GBM cell cultures under obstructed conditions. Under these conditions,

107   nutrient starvation leads to a chemotactic process and the formation of a migratory

108   front similar to the pseudopalisades observed in vivo and corresponding to predictive

109   mathematical algorithms. Moreover, our results suggest that the pseudopalisading

110   process stimulates a more aggressive behavior of GBM cells. This novel technique

111   could help us to understand the mechanism of pseudopalisade formation and to

112   suggest novel therapeutic targets to avoid tumor progression. These microfluidic

113   devices represent an extremely useful platform to evaluate cellular behavior and to test

114 new anticancer agents in a preclinical setting that mimics the complex GBM

115 microenvironment.

116

117 **METHODS**

118

119 **Microfluidic chip fabrication**

120 Microfluidic devices were fabricated using SU-8 photolithography combined with a SU-

121 8 to SU-8 bonding process. The fabrication process was inspired by previously

122 reported work describing the fabrication of SU-8 microdevices[12,13]. Briefly, several

123 layers of SU-8 were spun onto the Kapton film and different soft bake, UV exposure

124 and post-bake steps were performed[14,15].

125

126 **Packaging tool fabrication**

127 In order to recreate obstructed conditions (Fig 1A), a regular flow of culture media must

128 be provided to the microdevice through one lateral microchannel whereas the other is

129 sealed (Fig 1B). A dedicated package was designed and fabricated to provide proper

130 housing and hermetic connections to the microdevice inlets and outlets, allowing for

131 automated cellular culture. Final microdevice and packaging tool are showed in Fig.

132 1C.

133

134 **Cell culture**

135 C-6 cells were kindly provided by Dr Pešic (University of Belgrade) whereas U-251-MG

136 cells were purchased from ATCC. Both cells were routinely grown in Dulbecco´s

137 modified Eagle´s medium (DMEM) (Lonza BE12-614F) supplemented with 10% v/v

138 fetal bovine serum (Sigma F7524) and penicillin/streptomycin (DE 17-602E) within a

139 TEB-1000 incubator (EBERS Medical Technology). For three-dimensional cultures, all

140 reagents, microdevices included, were placed on ice. Cells were trypsinized and

141 resuspended in a calculated volume of medium (DMEM supplemented with 10 % fetal

142   bovine serum) to reach the desired concentration of cells in the final hydrogel solution.

143   Using a chilled tip, we prepared a mixture of 24.9 µl of collagen type I 4.01 mg/ml

144   (Corning 354236); 0.62 µl of NaOH 1N (Sigma 655104); 10 µl of DMEM 5X (Sigma

145   D5523), 50 µl of cell solution and 14.5 µl of sterile water. The hydrogel mixture was

146   injected into the device using a micropipette, then a 5 µl droplet was placed on top of

147   the central inlet to prevent hydrogel leakage and evaporation. Afterwards, the

148   microfluidic device was placed into an incubator (37°C and 5% CO_2) for 15 minutes to

149   allow collagen polymerization. For use as a macroscopic control on viability assays,

150   100 µl of hydrogel mixture was allowed to polymerize on Petri dishes. Medium within

151   microdevices was refreshed once a day. Cell membrane was fluorescently labelled

152   using vibrant Dil (Life Technologies, V-22885) following the supplier instructions.

153

154   **Cell Viability**

155   Stock solutions of 5 mg/ml Calcein (CAM) (Life technologies C1430) and 2 mg/ml

156   propidium iodide (PI) (Sigma P4170) were prepared following supplier instructions.

157

158   To test cell viability within microfluidic devices and in Petri dishes, stock solutions of

159   CAM and PI were diluted to 5 and 4 µg/ml, respectively, in phosphate-buffered saline

160   (PBS) (Lonza BE17-516F). Microdevices and petri controls were washed once with

161   PBS, and then filled with CAM/PI. Confocal images were immediately taken using a

162   Nikon Eclipse Ti microscope equipped with a C1 modular confocal microscope system.

163   Images were collected at different focal planes within each microdevice and Petri

164   control.

165

166   **Long-term cultures under obstructed conditions.**

167   To mimic the obstructed conditions, cells were embedded into a collagen hydrogel

168   injected within the central microchamber of the microdevices. After 24 hours, the

169   microdevices were loaded into the packaging tool and all inlets were sealed except for

170   one pair to enable medium perfusion through only one lateral microchannel (Fig. 1D).

171   As a control group, other microdevices were left on the Petri dish and medium was

172   manually refreshed once a day under unrestricted conditions. System evolution was

173   followed and cell viability and distribution was evaluated at different times. Flow profile

174   was characterized using green-fluorescent 0.2 µm diameter spheres (Life

175   Technologies, F8811). Oxygen profile across the microchamber was measured using

176   "Image-it Hypoxia reagent" (Life Technologies, H10498) dissolved in DMSO. Medium

177   supplemented with 10 µM hypoxia reagent was perfused through the system for 24

178   hours to ensure the reagent reached the microdevice. Continuous oxygen monitoring

179   throughout all the experiment was avoided due to the reagent toxicity. Hypoxia-induced

180   fluorescence was detected using a 488 nm laser coupled with a 650nm long-pass

181   detector in the confocal microscope.

182

183   **Glucose profile analysis**

184   The presence of a glucose gradient during experiments was studied using a

185   fluorescent glucose (2-NBDG) (Life Technologies N13195) which is imported by the

186   cells in place of glucose. Since 2-NBDG and conventional glucose compete for the cell

187   glucose transporters, cells were cultured within the microdevices in glucose-free

188   DMEM (Thermos Fisher Scientific, 11966-025) supplemented with fetal calf serum,

189   glutamine and antibiotics. This glucose-free medium was supplemented with 2-NBDG

190   at 200 µM and perfused through one lateral microchannel. Time-lapse images were

191   taken for 2 hours every 5 minutes to analyze NBDG penetration across the central

192   microchamber. Long-term experiments with NBDG and absence of conventional

193   glucose were not possible since it may affect cell behavior.

194

195   **Image analysis**

196   Cell analysis within the central microchamber and Petri controls was performed using

197   automated Fiji software (http://fiji.sc/Fiji). To analyze cell distribution within the central

198   microchamber, only focal planes ranging from 50 μm to 250 μm were used to exclude

199   cells attached directly to the 2D microchamber top and bottom. Selected focal planes

200   were flipped vertically, generating the orthogonal view, which was projected to get the

201   cell distribution across all the microchamber length. In order to analyze cell shape, cell

202   perimeter was drawn manually and ellipse fitted-aspect ratio was calculated as the ratio

203   between the ellipse major and minor axis. Cell directionality was also determined and

204   plotted as a histogram referred to the medium flow direction. At least one hundred cells

205   were analyzed in each region.

206

207   **Immunofluorescence**

208   Samples were fixed for 30 min with 4% paraformaldehyde (VWR J61899-AP),

209   permeabilized using 0,1% Triton-X100 (Sigma T8787) and blocked with 5% BSA

210   (Sigma A2058) in PBS. Samples were then incubated overnight with primary antibody

211   (1/50 in 2,5% BSA and 0,05% Triton X-100, Santacruz anti-Ki-67 sc-23900,), and

212   secondary antibody (1/200) was used under the same conditions. DAPI (Sigma D9542-

213   1MG) staining was performed overnight and after a washing step samples were

214   visualized.

215

216   **Tumor pathology**

217   The human tissues were procured after obtaining the patient written consent and with

218   the approval of the ethics committees of *Hospital Universitario 12 de Octubre*.

219   Hematoxylin-Eosyn (H&E) staining was performed on 5 μm thick sections from paraffin-

220   embedded tumors. Pseudopalisades areas were selected and the nuclear shape in the

221   rear end (close to the necrotic core) or at the front was calculated as previously

222   described. Twenty nuclei were analyzed in each region. Three different samples were

223   analyzed. All methods were carried out in accordance with the approved guidelines.

224

225   **Mathematical modeling**

226   This model is based on our previous models[10,16] where oxygen coming from straight

227   vessels was the driving force that triggered the normoxic and hypoxic phenotypic

228   changes. To these two dominant phenotypes, based on the go or grow dichotomy[17], we

229   have incorporated a third phenotype accounting for hypoxic cells that arrive to

230   normoxic areas and switch to a more proliferative phenotype. Also, in addition to the

231   diffusive random motion, we have comprised a directional transport term driving the

232   cell's motion towards better oxygenated regions for hypoxic cells that was not present

233   in Refs[10,16].

234

235   The mathematical model consists of a set of partial differential equations modelling the

236   interplay of three cellular cancer cell phenotypes, the oxygen distribution and necrosis:

237   *Major assumptions of the Mathematical Model:*

238   1. Hybrid model between *go or grow* and *go and grow* models.

239   2. Classical logistic space-limited growth for the tumor cell populations.

240   3. Hypoxic phenotype is more migratory than any other cell phenotype.

241   4. Oxygen acts as a chemoattractant for hypoxic cells.

242   5. Malignant cells have the highest proliferation.

243   6. Homogenous and isotropic oxygen diffusion in the chamber.

244   7. Oxygen flows from channels to balance the different oxygen pressures.

245   8. Malignant cells consume more oxygen than any other cell phenotype.

246

247   **Statistical analysis**

248   Data were analyzed using SPSS software, and statistical significance was set at $p <$

249   0.05. Results are presented as mean ± standard error. The normal distribution was

250   tested by the Kolmogorov-Smirnov test. For parametric comparison, one way ANOVA

251   with Bonferroni post hoc tests was performed. For nonparametric comparisons, a

252   Kruskal-Wallis test was performed followed by the U-test of Mann-Whitney.

253

RESULTS

255

GBM cells are viable in 3-dimensional microchamber culture

The fabricated microdevice possesses a central microchamber to locate the cells embedded within a hydrogel[18-20], mimicking the ECM and allowing migration in three dimensions. On both sides of the microchamber, lateral microchannels are filled with culture medium, allowing nutrient and oxygen diffusion throughout the microchamber, mimicking the function of brain blood vessels.

262

We first examined microdevice biocompatibility with GBM cells to ensure the material does not affect cell viability. After 7 days in culture, we evaluated U-251 cell viability within microdevices compared to culture dish controls using CAM and propidium iodide (PI). Results showed that cell viability within microdevices was very high (>95%) and more importantly it was similar to culture controls at the same timepoint, validating the use of this microdevice for three dimensional U-251 cell culture (Fig. 1E, F).

269

Flow profile

Culture medium supplemented with 1% spheres suspension was injected through the lateral microchannel in obstructed conditions to study the flow profile. Fluorescent time-lapse images demonstrated that under obstructed conditions the flow profile was not penetrating into the hydrogel (Supporting Fig. 1A-C), but it was completely parallel to the central microchamber. When an interstitial flow through the central microchamber was externally imposed, the fluorescent spheres invaded the hydrogel in few minutes (Supporting Fig. 1D-F). Therefore, under obstructed conditions the fluid flow is not mechanically affecting the hydrogel or the embedded cells.

279

GBM cells migrate under obstructed conditions

281 By controlling medium flow through the lateral microchannels, we can mimic the GBM-

282 associated thrombotic pathophysiological conditions. Under unrestricted conditions, cell

283 distribution within the microchamber was constant throughout the experiment (nine

284 days of culture, Fig. 2A-C). Under obstructed conditions, cell viability continued to be

285 very high (>95%) and we also observed a strong migratory process. After three days of

286 thrombotic conditions, cell migration was barely apparent and only small cell

287 aggregates near the perfused microchannel were visible (Fig. 2D). After six days,

288 migration evolved to the formation of a well-defined front, resembling the in vivo

289 observed pseudopalisades (Fig. 2E). Finally, after nine days this front moved closer to

290 and invaded the perfused microchannel (Fig. 2F). In order to perform a more

291 quantitative and precise analysis, we analyzed the fluorescence intensity across the

292 microchamber. This analysis of cell distribution confirmed that under unrestricted

293 conditions there was no change during the time course (Fig. 2G). On the other hand,

294 after three days under obstructed conditions this distribution showed a moderate

295 increase nearby the perfused lateral microchannel compared to the unrestricted

296 conditions, showing an emerging migratory response (Fig. 2H). After six days, this

297 response increased to a well-defined peak, indicating cells concentrating in this region,

298 creating the characteristic pseudopalisade front and abandoning the occluded rear

299 region. After nine days, the intensity of the pseudopalisade front reached a maximum

300 and was displaced as cells reached the perfused lateral microchannel. This is the first

301 experimental evidence showing the creation of a pseudopalisade front by a migratory

302 wave of GBM cells moving from obstructed to perfused conditions. In order to expand

303 this study using another GBM cell line, C-6 cells were cultured in the microdevice under

304 similar conditions. After 3 days under obstructed conditions, C-6 cells showed an

305 invasion process towards the perfused lateral microchannel (Supporting Fig. 2).

306 Interestingly, C-6 cells exhibited a faster invasion than U-251 MG. Furthermore, a

307 population of dead C-6 cells appeared concentrated nearby the obstructed lateral

308 microchannel. Thereby, C-6 cells seemed to have a faster metabolism compared with

309   U-251 MG, which led to an accelerated invasion. Longer invasion times using C-6 cells

310   were not analyzed due to a significant hydrogel contraction caused by these cells.

311

312   **Cell morphology analysis during pseudopalisade formation**

313   Our results suggested that pseudopalisading structures can be created by a migratory

314   response lead by cells located at the rear of the migratory front, near the non-perfused

315   microchannel. We next investigated the morphologic changes in GBM cells during the

316   formation of pseudopalisades. As expected, after 5 days of culture cells under

317   unrestricted conditions appeared identical on either side of the microchamber (Fig. 3A).

318   Conversely, five days after the induction of obstructed conditions cell morphology

319   clearly shifted in the cell population closest to the obstructed channel (Fig. 3B). In the

320   rear, cells greatly increased in aspect ratio (5.3 ± 2.3) and became highly elongated

321   with very large protrusions, whereas in the front cells were mainly rounded with aspect

322   ratio close to one (1.2 ± 0.2) (p-value < 0.001) (Fig. 3C). We analyzed cell directionality

323   near the obstructed channel and found a bias towards the medium flow (Fig. 3D). Cell

324   directionality in those regions with lower aspect ratio (≈1) was not analyzed, since this

325   parameter is irrelevant in rounded cells. Interestingly we observed the same cellular

326   pattern in the pseudopalisades detected in human GBM samples, with a significant

327   change in the nucleus aspect ratio (2.1 ± 0.5) in the rear end (close to the necrotic

328   core) compared to the front (1.3 ± 0.2) (Fig. 3E and F).

329

330   **Characterization of pseudopalisade formation**

331   A recent hypothesis about GBM suggests that when migrating cells forming the

332   pseudopalisade reach a new nutrient rich microenvironment (i.e. in the vicinity of a

333   perfused blood vessel) their metabolism changes back to a more proliferative and less

334   migratory state. To test this hypothesis within our system, we analyzed cell proliferation

335   under the different stages of pseudopalisade formation by Ki-67 immunofluorescence.

336   After 5 days under obstructed conditions, we observed no Ki-67 positive cells (Fig. 4A).

337   On the other hand, when the pseudopalisade was completely formed after 9 days

338   under obstructed conditions, positive cells were observed (Fig. 4B). More interestingly,

339   those proliferative cells appeared only in the vicinities of the perfused microchannel

340   where nutrient concentrations are expected to be highest. Under unrestricted

341   conditions we did not observed positive cells either after 5 or after 9 days (Fig. 4C and

342   D). Central microchamber was vertically divided in three regions and the number of

343   proliferating cell was determined in each one (Fig 4E). The analysis demonstrated most

344   of the proliferating cells were located on the region closest to the perfused lateral

345   microchannel, only a small proportion appeared in the central region, and no

346   proliferating cells were observed in the further region.

347   To determine if a glucose gradient was generated during long-term experiments, we

348   analyzed the diffusion profile of the fluorescent glucose analog 2-deoxy-2-[(7-nitro-

349   2,1,3-benzoxadiazol-4-yl)amino]-D-glucose (NBDG) across the microchamber in the

350   absence or presence of cells (Supporting Fig. 3) during 2 hours post-NBDG injection.

351   We found little difference in cellular glucose uptake across the microchamber and cells

352   were able to uptake the NBDG. The NBDG diffusion profile without cells (green line)

353   was very similar to the NBDG with cells curve (red line). (Note: the dark areas

354   observed in the assay containing cells are due to light scattering from cells out of the

355   focal plane. Supporting Fig. 4). After removing the NBDG, cell remained labelled in

356   green, showing their ability to incorporate the glucose analog (Supporting Fig. 5). This

357   indicates that during long-term experiments GBM cells are not exposed to a significant

358   glucose gradient and further suggests that pseudopallisading formation is driven by

359   factors other than glucose scarcity.

360   We next investigated the oxygen profile across the microchamber during experiments

361   using Image-it hypoxia reagent which becomes fluorescent as oxygen tension

362   decreases. Two different sets of experiments were performed, both carried out for 5

363   days: Under unrestricted conditions medium was pipetted only once a day through both

364   lateral microchannels. Since both lateral microchannels remained open, the oxygen

365   consumption was symmetric; thereby, a homogeneous hypoxia along the

366   microchamber was generated (Fig 5A and Supporting Fig 6A).

367   On the other hand, under obstructed conditions the medium flow through the right

368   lateral microchannel guaranteed that oxygen and nutrients in the perfused lateral

369   microchannel were continuously refreshed; whereas the opposed lateral microchannel

370   remained blocked. Thereby, those cells located nearby to the perfused microchannel

371   showed very low hypoxia-induced fluorescence intensity, suggesting a normoxic

372   microenvironment; whereas those cells located nearby the blocked microchannel

373   showed the highest hypoxia-induced fluorescence intensity (Fig 5B, C and Supporting

374   Fig 5B).

375   These results suggested that gradient conditions were needed to induce the directional

376   migratory process, since under "unrestricted conditions" no directional migration was

377   observed even when a homogenous hypoxia was observed.

378

379   **Correlation of computer simulations with experimental data**

380   Since the migratory response of the GBM cells is non-linear and not entirely intuitive,

381   we investigated the correlation of our experimental data with simulated computer

382   models. Under unrestricted conditions, the number of cells and their distribution along

383   the chamber vary only slightly due to the very slow proliferation rates we observe (Fig

384   6A). In our computer simulations, all cells have a normoxic phenotype after 9 days.

385   When the nutrient flow along the left channel was disrupted, cellularity remained

386   spatially homogeneous for 3 days while the nutrient level becomes exhausted, after

387   which cells slowly change their phenotypes. However, our numerical simulations reveal

388   the formation of a pseudopalisade structure moving towards the active channel after 6

389   days and a dramatic increase in cell density around the flow channel at day 9 (Fig. 6B),

390   which is strongly in agreement with our experiments. Fig. 8C shows the mathematical

391   model scheme used in the computational simulations. We have performed an

392   extensive parameter value scans and we are forced to conclude that the dynamic

393   behavior observed in our experimental model cannot be reproduced within the

394   framework of the previously published two-phenotype computational model[10,16] which

395   assumes that tumor cells revert to their original normoxic phenotypes when reaching

396   areas of higher oxygenation. Instead, the incorporation of a third highly proliferative

397   phenotype after the wave of migration is essential to reproduce the evolution of our

398   observed cell density profiles during pseudopalisade generation. Our analysis suggests

399   the existence of a highly proliferative GBM cell state triggered by transient waves of

400   metabolic deprivation and migration (Figure 6C).

401

402   **DISCUSSION**

403

404   Nutrient and oxygen depletion due to blood vessel obstruction events play an important

405   role on the accelerated spreading of GBM cells across the brain. In this work, we

406   provide a robust and novel methodology to mimic the GBM-associated blood vessel

407   obstruction in vitro. Using our developed microdevice, we were able to culture GBM

408   cells under induced obstructed conditions and for the first time we can demonstrate the

409   formation of a pseudopalisade-like front through several sequential steps. In an initial

410   stage, during the first days under obstructed conditions, there is little morphologic

411   change in the GBM cells as remaining oxygen and nutrients are consumed. In a

412   second stage, nutrient starvation leads to an intense migratory response in those cells

413   located in the starved region, i.e. the pseudopalisade rear. This migratory response

414   creates the observed pseudopalisading structures after six days in culture. Finally, in a

415   third stage, cells of this pseudopalisade front reach the nutrient source (invading the

416   perfused lateral microchannel) and undergo rapid proliferation. This behavior models

417   GBM pseudopalisade progression observed in patients and enables the study of this

418   phenomenon in vitro. The pseudopalisading hypothesis has been suggested to explain

419   the poor improvement on mean survival time achieved by conventional anti-tumorigenic

420 treatments[21]. Accordingly, the approved chemotherapy treatment for GBM, based on

421 concomitant doses of the alkylating chemotherapy agent temozolomide combined with

422 radiotherapy, only improves mean survival time by a few months compared with

423 radiotherapy only[1,21]. Since most such treatments are focused on killing proliferative

424 cells they do not target those non-proliferative migratory cells of pseudopalisades.

425 Unfortunately, once these cells reach nutrient rich regions they can again become

426 proliferative.

427

428 Many recent reports show that cell migration palys a critical role on GBM invasion and

429 spreading, and correlates with patient prognosis[22-24]. In this context, new drugs are

430 being developed to block GBM cells migration[25]. Thus, different animal and in vitro

431 studies show that treatment with specific migration inhibitors can achieve a significantly

432 mean survival time improvement[26,27]. It has been shown GBM cells invade by a

433 mesenchymal migration mode[28-30] based on integrins and matrix degrading enzymes

434 like membrane type matrix metalloproteinase-1 (MT-MMP-1) and MMP-2 [31,32]. These

435 proteins normally are overexpressed in GBM[33]. More interestingly, recent reports have

436 shown hypoxia, through HIF-1α, induce an epithelial-mesenchymal transition (EMT) in

437 GBM cell lines, enhancing cell invasiveness[34]. In our model, cells showed this expected

438 mesenchymal-like GBM migration mode, including the characteristic emission of

439 invadopodia and very large aspect ratio[35]. Our directionality distribution showed that

440 rear cells were preferentially orientated towards the perfused lateral microchannel (the

441 oxygen and nutrient source), forming an angle of 90° with medium flow and aligning in

442 the direction of travel during pseudopalisade formation.

443

444 Our oxygen profile measurements reveal that under obstructed conditions cell

445 metabolism creates an oxygen gradient across the microchamber, resembling the

446 hypoxic areas observed in in-vivo pseudopalisades. Our mathematical model suggests

447 the development of a more malignant phenotype after these cycles of hypoxia,

448 migration, and re-oxygenation. This phenotype is highly proliferative and oxygen

449 dependent. Our mathematical simulations support the hypothesis of pseudopalisade

450 formation after a vessel occlusion event and correlate very well with microfluidic device

451 experiments, in which we saw an increase in the cell proliferation when the cells where

452 exposed to obstructed conditions. Our results suggest that both the enhanced

453 infiltration and the malignant phenotype arising after hypoxic cells reach better

454 oxygenated areas may be relevant tumor driving forces originated by microscopic

455 hypoxic events. Therefore, this mathematical model is able to recapitulate the

456 pseudopalisade formation as a hypoxia-driven phenomenon, convincingly reproducing

457 the observed results within the microdevice and the observed pseudopalisades in vivo.

458

459 Our interdisciplinary approach now allows direct observation of GBM invasion and

460 pseudopalisade formation under controlled conditions. Furthermore, the mathematical

461 modeling suggests a sequence of cell states which include alternating phases of

462 hypoxia, invasiveness, and proliferation. These methodologies enable us to see

463 processes once only found in vivo, shed light on the states and life cycle of GBM, and

464 could enable more biologically accurate drug screening methods focused on GBM

465 invasion.

466

467 **ACKNOWLEDGMENTS**

484

485

REFERENCES

1. Oike T, Suzuki Y, Sugawara K, et al. Radiotherapy plus concomitant adjuvant temozolomide for glioblastoma: Japanese mono-institutional results. *PloS one.* 2013; 8(11):e78943.

2. Brat DJ. Glioblastoma: biology, genetics, and behavior. *American Society of Clinical Oncology educational book / ASCO. American Society of Clinical Oncology. Meeting.* 2012:102-107.

3. Rong Y, Durden DL, Van Meir EG, Brat DJ. 'Pseudopalisading' necrosis in glioblastoma: a familiar morphologic feature that links vascular pathology, hypoxia, and angiogenesis. *Journal of neuropathology and experimental neurology.* 2006; 65(6):529-539.

4. Brat DJ, Castellano-Sanchez AA, Hunter SB, et al. Pseudopalisades in glioblastoma are hypoxic, express extracellular matrix proteases, and are formed by an actively migrating cell population. *Cancer research.* 2004; 64(3):920-927.

5. Wippold FJ, 2nd, Lammle M, Anatelli F, Lennerz J, Perry A. Neuropathology for the neuroradiologist: palisades and pseudopalisades. *AJNR. American journal of neuroradiology.* 2006; 27(10):2037-2041.

6. Rong Y, Post DE, Pieper RO, Durden DL, Van Meir EG, Brat DJ. PTEN and hypoxia regulate tissue factor expression and plasma coagulation by glioblastoma. *Cancer research.* 2005; 65(4):1406-1413.

7. Brat DJ, Van Meir EG. Vaso-occlusive and prothrombotic mechanisms associated with tumor hypoxia, necrosis, and accelerated growth in glioblastoma. *Laboratory investigation; a journal of technical methods and pathology.* 2004; 84(4):397-405.

509   **8.**   Jensen RL. Brain tumor hypoxia: tumorigenesis, angiogenesis, imaging,

510   pseudoprogression, and as a therapeutic target. *Journal of neuro-oncology.* 2009;

511   92(3):317-335.

512   **9.**   Jain RK, di Tomaso E, Duda DG, Loeffler JS, Sorensen AG, Batchelor TT. Angiogenesis in

513   brain tumours. *Nat Rev Neurosci.* 2007; 8(8):610-622.

514   **10.**   Martinez-Gonzalez A, Calvo GF, Perez Romasanta LA, Perez-Garcia VM. Hypoxic cell

515   waves around necrotic cores in glioblastoma: a biomathematical model and its

516   therapeutic implications. *Bulletin of mathematical biology.* 2012; 74(12):2875-2896.

517   **11.**   Bhatia SN, Ingber DE. Microfluidic organs-on-chips. *Nature biotechnology.* 2014;

518   32(8):760-772.

519   **12.**   Blanco FJ, Agirregabiria M, Garcia J, et al. Novel three-dimensional embedded SU-8

520   microchannels fabricated using a low temperature full wafer adhesive bonding.

521   *Micromechanics and Microengineering.* 2004; 14(7):10.

522   **13.**   Ayuso JM, Monge R, Llamazares G, et al. SU-8 based microdevices to study self-

523   induced chemotaxis in 3D microenvironments. *Front Mater.* 2015; 2: 37(37).

524   **14.**   Altuna A, Bellistri E, Cid E, et al. SU-8 based microprobes for simultaneous neural

525   depth recording and drug delivery in the brain. *Lab on a chip.* 2013; 13(7):1422-1430.

526   **15.**   Altuna A, Menendez de la Prida L, Bellistri E, et al. SU-8 based microprobes with

527   integrated planar electrodes for enhanced neural depth recording. *Biosensors &*

528   *bioelectronics.* 2012; 37(1):1-5.

529   **16.**   Martinez-Gonzalez A, Duran-Prado M, Calvo GF, Alcain FJ, Perez-Romasanta LA, Perez-

530   Garcia VM. Combined therapies of antithrombotics and antioxidants delay in silico

531   brain tumour progression. *Mathematical medicine and biology : a journal of the IMA.*

532   2014.

533   **17.**   Hatzikirou H, Basanta D, Simon M, Schaller K, Deutsch A. 'Go or grow': the key to the

534   emergence of invasion in tumour progression? *Mathematical medicine and biology : a*

535   *journal of the IMA.* 2012; 29(1):49-65.

536   **18.**   Jeong GS, Han S, Shin Y, et al. Sprouting angiogenesis under a chemical gradient

537   regulated by interactions with an endothelial monolayer in a microfluidic platform.

538   *Analytical chemistry.* 2011; 83(22):8454-8459.

539   **19.**   Kim C, Kasuya J, Jeon J, Chung S, Kamm RD. A quantitative microfluidic angiogenesis

540   screen for studying anti-angiogenic therapeutic drugs. *Lab on a chip.* 2015; 15(1):301-

541   310.

542   **20.**   Kothapalli CR, van Veen E, de Valence S, et al. A high-throughput microfluidic assay to

543   study neurite response to growth factor gradients. *Lab on a chip.* 2011; 11(3):497-507.

544   **21.**   Peponi E, Tourkantonis I, Tasiou I, Pavlidis N, Pentheroudakis G, Tsekeris P. Prognostic

545   factors in glioblastoma patients managed with radiotherapy combined with

546   temozolomide. *Journal of B.U.ON. : official journal of the Balkan Union of Oncology.*

547   2014; 19(3):718-723.

548   **22.**   Vehlow A, Cordes N. Invasion as target for therapy of glioblastoma multiforme.

549   *Biochimica et biophysica acta.* 2013; 1836(2):236-244.

550   **23.**   Moller HG, Rasmussen AP, Andersen HH, Johnsen KB, Henriksen M, Duroux M. A

551   systematic review of microRNA in glioblastoma multiforme: micro-modulators in the

552   mesenchymal mode of migration and invasion. *Mol Neurobiol.* 2013; 47(1):131-144.

553   **24.**   Lefranc F, Brotchi J, Kiss R. Possible future issues in the treatment of glioblastomas:

554   special emphasis on cell migration and the resistance of migrating glioblastoma cells to

555   apoptosis. *Journal of clinical oncology : official journal of the American Society of*

556   *Clinical Oncology.* 2005; 23(10):2411-2422.

557   **25.**   Scaringi C, Minniti G, Caporello P, Enrici RM. Integrin inhibitor cilengitide for the

558   treatment of glioblastoma: a brief overview of current clinical results. *Anticancer*

559   *research.* 2012; 32(10):4213-4223.

560   **26.**   Munson JM, Fried L, Rowson SA, et al. Anti-invasive adjuvant therapy with imipramine

561   blue enhances chemotherapeutic efficacy against glioma. *Science translational*

562   *medicine.* 2012; 4(127):127ra136.

563   **27.**   Zhang L, Wang H, Zhu J, Ding K, Xu J. FTY720 reduces migration and invasion of human

564   glioblastoma cell lines via inhibiting the PI3K/AKT/mTOR/p70S6K signaling pathway.

565   *Tumour biology : the journal of the International Society for Oncodevelopmental*

566   *Biology and Medicine.* 2014.

567   **28.**   Myung JK, Choi SA, Kim SK, Wang KC, Park SH. Snail plays an oncogenic role in

568   glioblastoma by promoting epithelial mesenchymal transition. *International journal of*

569   *clinical and experimental pathology.* 2014; 7(5):1977-1987.

570   **29.**   Piao Y, Liang J, Holmes L, Henry V, Sulman E, de Groot JF. Acquired resistance to anti-

571   VEGF therapy in glioblastoma is associated with a mesenchymal transition. *Clinical*

572   *cancer research : an official journal of the American Association for Cancer Research.*

573   2013; 19(16):4392-4403.

574   **30.**   Caspani EM, Echevarria D, Rottner K, Small JV. Live imaging of glioblastoma cells in

575   brain tissue shows requirement of actin bundles for migration. *Neuron Glia Biol.* 2006;

576   2(2):105-114.

577   **31.**   Hotary K, Allen E, Punturieri A, Yana I, Weiss SJ. Regulation of cell invasion and

578   morphogenesis in a three-dimensional type I collagen matrix by membrane-type

579   matrix metalloproteinases 1, 2, and 3. *The Journal of cell biology.* 2000; 149(6):1309-

580   1323.

581   **32.**   Friedl P. Prespecification and plasticity: shifting mechanisms of cell migration. *Current*

582   *opinion in cell biology.* 2004; 16(1):14-23.

583   **33.**   Yamamoto M, Ueno Y, Hayashi S, Fukushima T. The role of proteolysis in tumor

584   invasiveness in glioblastoma and metastatic brain tumors. *Anticancer research.* 2002;

585   22(6C):4265-4268.

586   **34.**   Joseph JV, Conroy S, Pavlov K, et al. Hypoxia enhances migration and invasion in

587   glioblastoma by promoting a mesenchymal shift mediated by the HIF1alpha-ZEB1 axis.

588   *Cancer letters.* 2015.

589   **35.**   Yilmaz M, Christofori G, Lehembre F. Distinct mechanisms of tumor invasion and

590   metastasis. *Trends in molecular medicine.* 2007; 13(12):535-541.

591

592

593

594

595

596

597   **Fig 1. Experimental set-up.** A) Scheme of pseudopalisade formation. Under

598   obstructed conditions, nutrient scarcity triggers a migratory response in those cells

599   located in the obstructed blood vessel vicinity (I) towards enriched regions (II). B)

600   Experimental scheme within the microdevice, mimicking the obstructed conditions and

601   the starved (I) and enriched (II) region. C) Fabricated microdevice and packaging tool.

602   D) Microfluidic system. E) U-251 cell viability within the microdevice after 9 days, live

603   cells (labelled with Calcein 1 µg/ml) are shown in green whereas dead cells are in red

604   (labelled with Propidium iodide 4 µg/ml). Microdevice posts (50x100 µm) are delimited

605   in white dashed line. Cells were cultured at 4 million cells/ml within a 1.5 mg/ml

606   collagen hydrogel. Viable cells are shown in green, whereas dead ones are in red. F)

607   Cell viability comparison between hydrogels on Petri dishes (red) and within the

608   microdevice (blue). Cell viability is expressed as the percentage of live cells. Scale bar

609   is 200 µm.

610

611   **Fig 2. Pseudopalisade formation under obstructed conditions.** U-251 at 4 million

612   cells/ml in collagen hydrogel at 1.5 mg/ml were culture within microdevices. Under

613   unrestricted conditions medium was refreshed once a day and cell viability was

614   evaluated at three (A), six (B) and nine (C) days using Calcein (green) and propidium

615   iodide (red). To mimic obstructed conditions, medium flow was enabled only through

616   right microchannel and cell viability was assessed at three (D), six (E) and nine (F)

617   days. Microdevice posts (50x100 µm) are delimited in white dashed line. Graphs show

618   the fluorescence intensity across the microchamber orthogonal view at three (G), six

619 (H) and nine days (I) in obstructed as unrestricted conditions. Post position in the

620 graphs is delimited by gray dashed line. Scale bar is 200 μm.

621 **Fig 3. Cell shape during Pseudopalisade formation.** Confocal images of the

622 microchamber after five days in culture under unrestricted (A) or obstructed conditions

623 were taken (B). C) Cell shape at the pseudopalisade rear and front was analyzed and

624 compared with the same region under unrestricted conditions, *** denotes a statistical

625 difference (p-value 1.4×10^{-32}). D) Directionality at the pseudopalisade rear under

626 obstructed conditions. E) H&E staining of a paraffin-embedded GBM sample. F)

627 Nucleus aspect ratio in the pseudopalisade rear and front in patient samples, ***

628 denotes a statistical difference (p-value 3.7×10^{-8}). Scale bar is 200 μm.

629 **Fig 4. Proliferation during pseudopalisade formation.** Ki-67 immunofluorescence

630 was performed within the microdevices during the different steps of the pseudopalisade

631 formation. A-B) Under obstructed conditions, ki-67 positive cells were observed only

632 after 9 days, when the pseudopalisade was completely formed. C-D) Under

633 unrestricted conditions no positive cells were observed at 5 or 9 days. Scale bar is 200

634 μm.

635 **Fig 5. Oxygen profile.** Oxygen profile was detected after 5 days in culture using

636 Image-it Hypoxia reagent and images are shown as heat-map hypoxia-induced

637 fluorescence intensity. Hypoxia-induced fluorescence intensity across the

638 microchamber revealed oxygen concentration was constant under unrestricted

639 conditions (A), whereas under obstructed conditions an oxygen gradient was

640 established (B). The graph shows the hypoxia-induced fluorescence intensity profile

641 across the microchamber (C). Scale bar is 200 μm.

642 **Fig 6. Computer simulations versus experimental data of the cell evolution**

643 **profiles.** Simulations of tumor cell density evolution and experimental data of

644 fluorescence intensity within the chamber under unrestricted conditions (A) and under

645   obstructed conditions (B). Left Y axis denotes fluorescence intensity from experiments

646   at day 3, 6 and 9, curves red blue and black respectively. Right Y axis denotes cell

647   density from simulations at day 3, 6 and 9, red spots, blue cross and black circles

648   respectively. Post position in the graphs is delimited by gray dashed line. C) Graphical

649   depiction of the mathematical model scheme based on previous models [10, 13] and

650   including three cancer cell phenotypes, the oxygenation and the necrosis (C).

651

652 **Fig 1.**
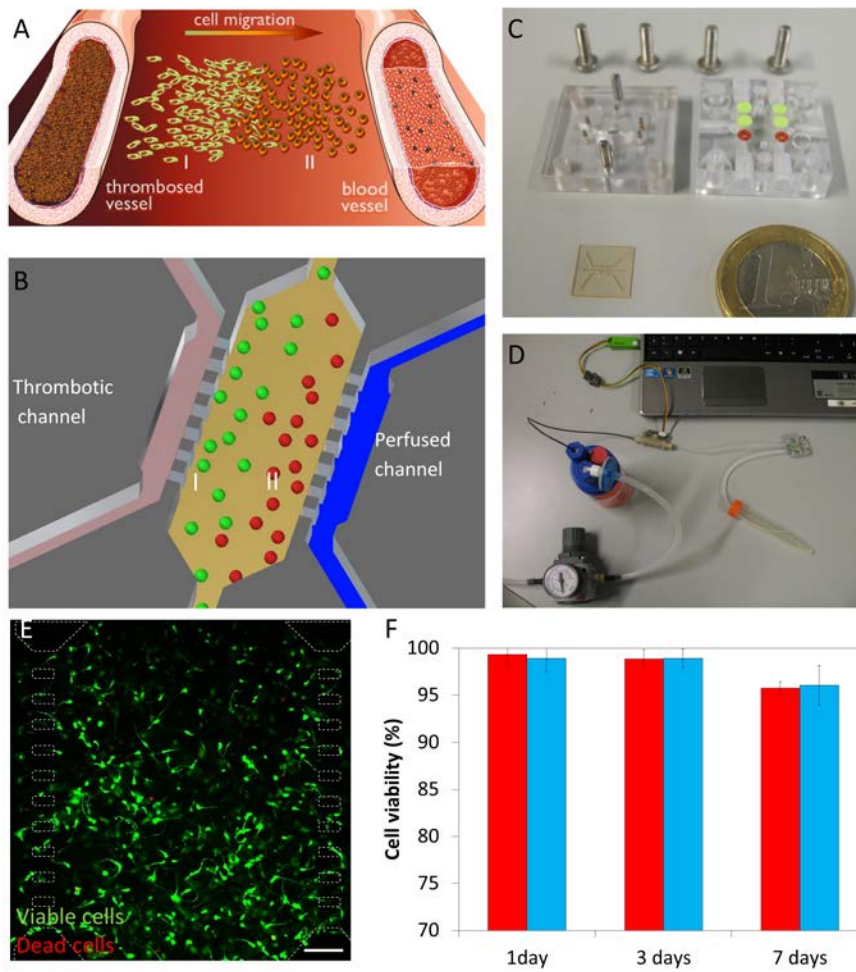
653

654

655   **Fig 2.**
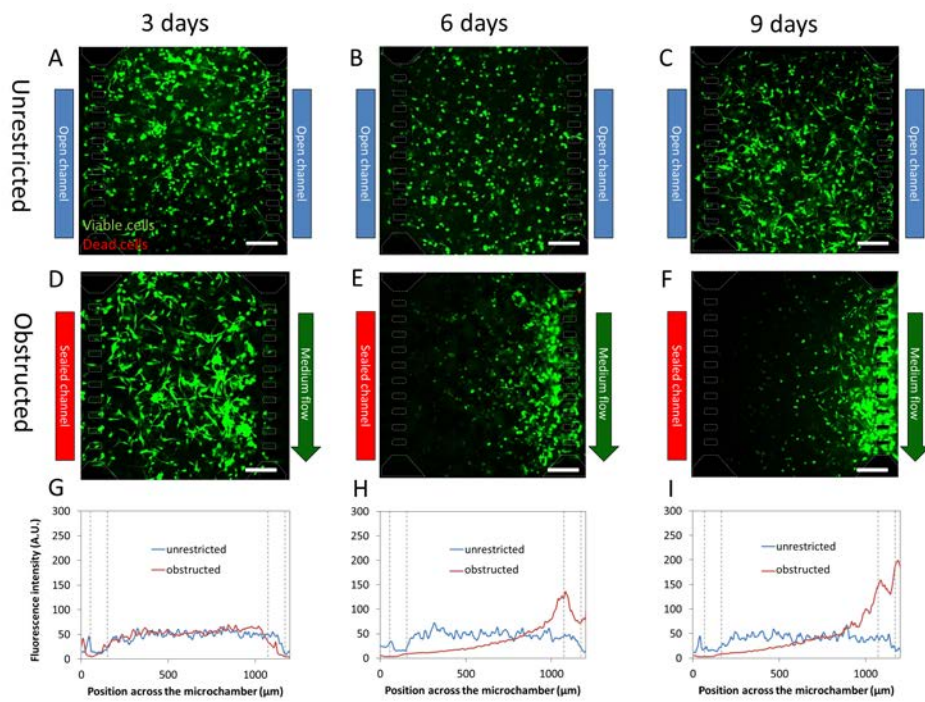
656

657

658   **Fig 3.**
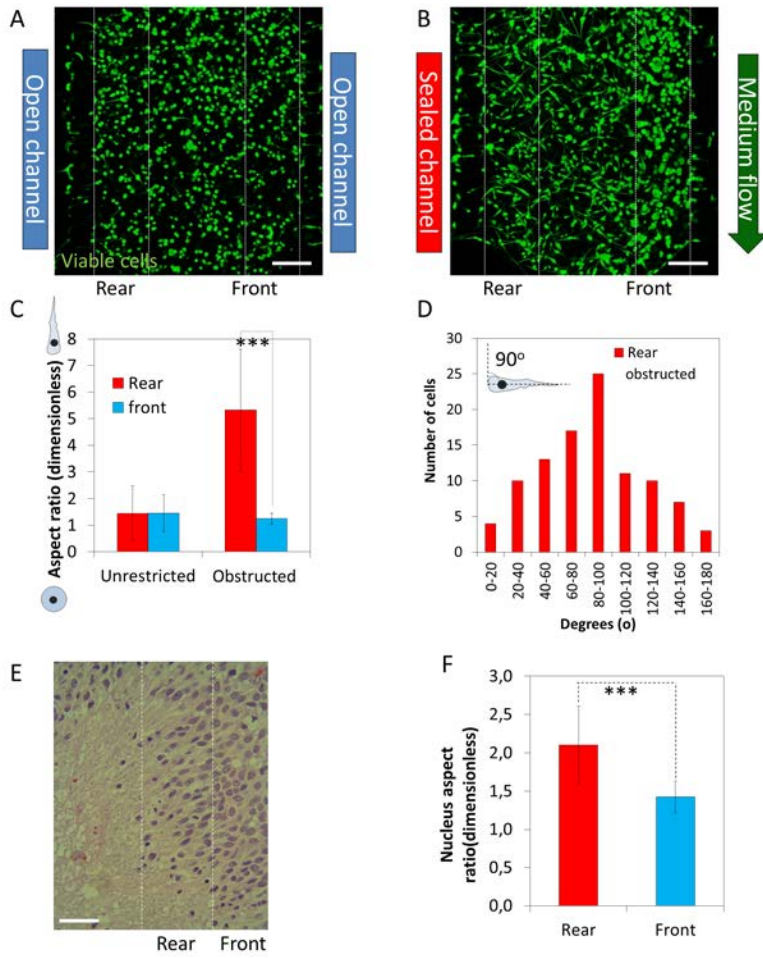
659

660

661   **Fig 4.**
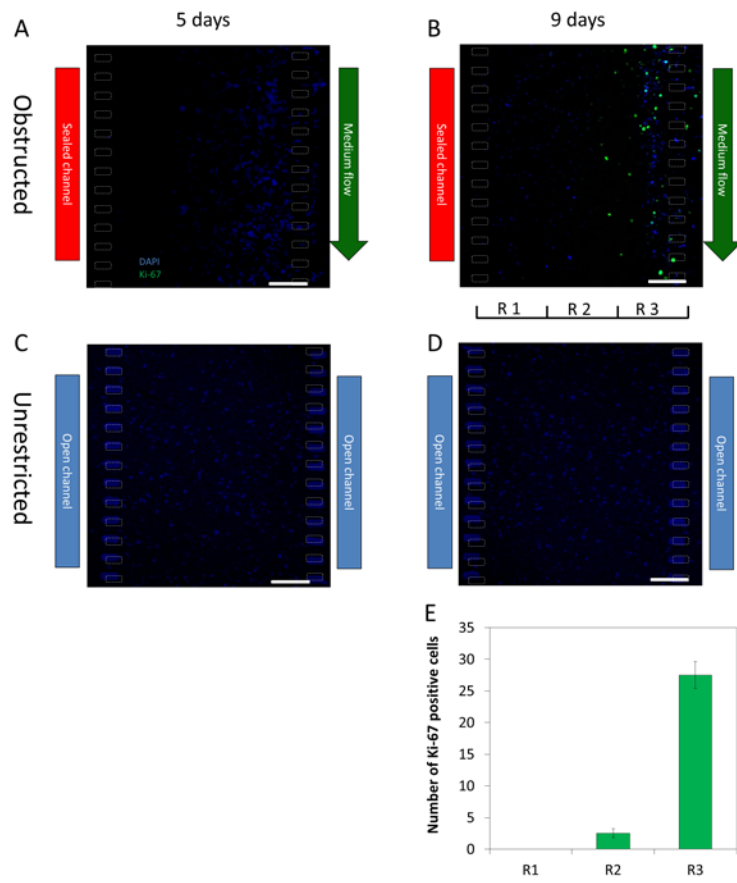
662

663

664

665

666   **Fig 5.**
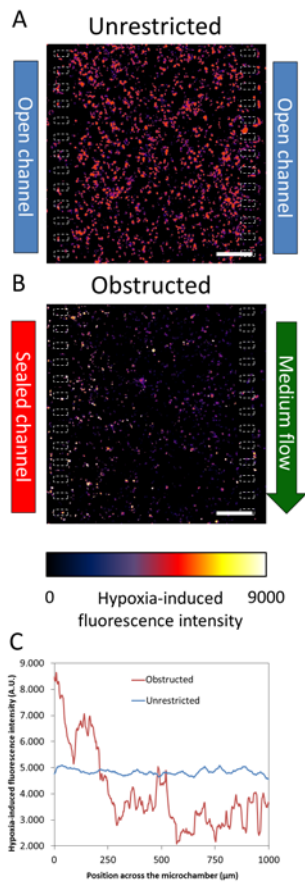
667

668

669

670

671

672 **Fig 6.**
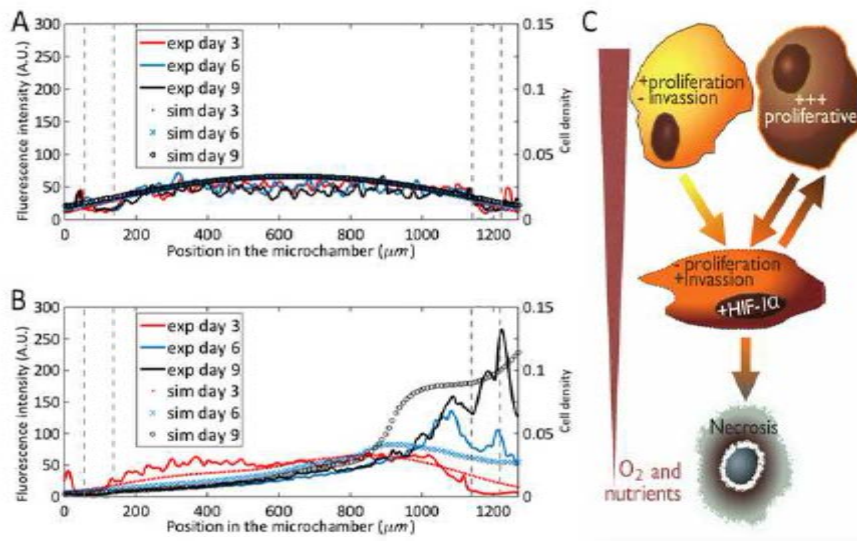
673

674

675   **Supporting Fig 1. Flow characterization.** Green-fluorescent spheres were dissolved

676   in the culture medium to study the flow profile during long-term experiments under

677   obstructed conditions. A-C) Fluorescent time-lapse images during obstructed

678   conditions showed no sphere penetration in the hydrogel. D-F) Interstitial flow through

679   the hydrogel was created opening one of the inlets of the "sealed" lateral microchannel

680   and closing one of the "perfused" one to illustrate the fluorescent spheres penetration.

681   Scale bar is 200 μm.

682   **Supporting Fig 2. C6 cells cultured within the microdevices.** 4 million C6 GBM

683   cells/ml were embedded in a 1.2 mg/ml collagen hydrogel and confined in the central

684   microchamber. Microdevices were cultured under unrestricted conditions (A) or

685   obstructed conditions (B). After 3 days, cell viability was analyzed with CAM/PI

686   staining; showing viable cells in green and dead ones in red. Graphs show the

687   viable/dead cell fluorescence intensity distribution along the delimited region (yellow

688   rectangle in the images). Pillar position is shown in dashed line. Scale bar is 200 μm.

689   **Supporting Fig 3. Glucose profile.** Glucose-free culture medium supplemented with

690   200 μm NBDG was perfused through the lateral microchannel. Cells were fluorescently

691   labelled in red and the NBDG diffusion profile was studied in the presence (red line)

692   and absence (green line) of cells after 10 (A), 60 (B) and 120 (C) min. Scale bar is 200

693   μm.

694   **Supporting Fig 4. NBDG diffusion profile.** During NBDG diffusion, dark spots were

695   observed within the hydrogel when Dil-labelled cells were present. Those spots

696   corresponded to cells out of focus that caused green-light scattering. Scale bar is 200

697   μm.

698   **Supporting Fig 5. NBDG uptake**. After perfusing NBDG through the right

699   microchannel, growth medium was perfused through the system to remove the NBDG.

700   Dil-labelled cells remained fluorescent in the hydrogel, and now green fluorescent was

701   observed within the cells, demonstrating their ability to incorporate the NBDG. Scale

702   bar is 200 μm.

703   **Supporting Fig 6. Oxygen profile.** Oxygen profile was detected after 5 days in culture

704   using Image-it Hypoxia reagent. Hypoxia-induced fluorescence intensity across the

705   microchamber revealed oxygen concentration was constant under unrestricted

706   conditions (A), whereas under obstructed conditions an oxygen gradient was

707   established (B). Scale bar is 200 μm.

708

709   **Supporting Fig 1.**
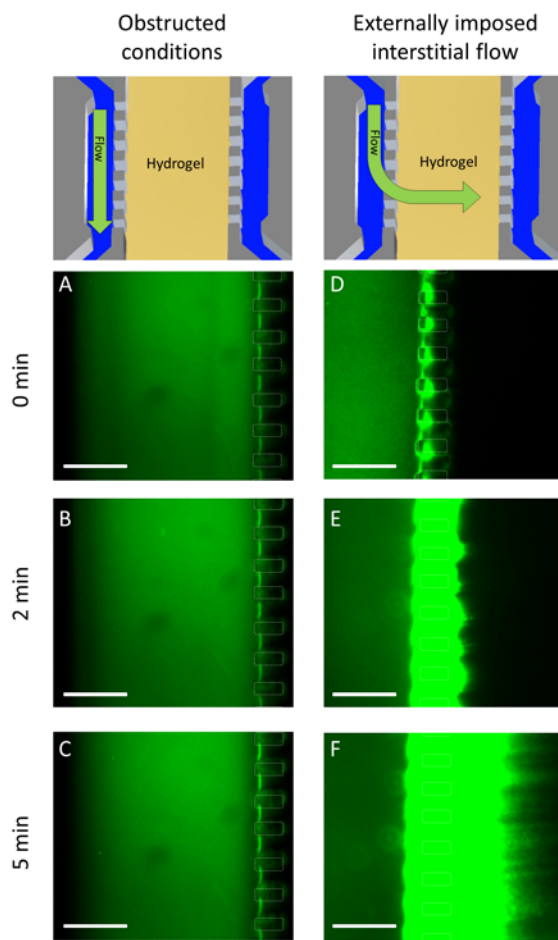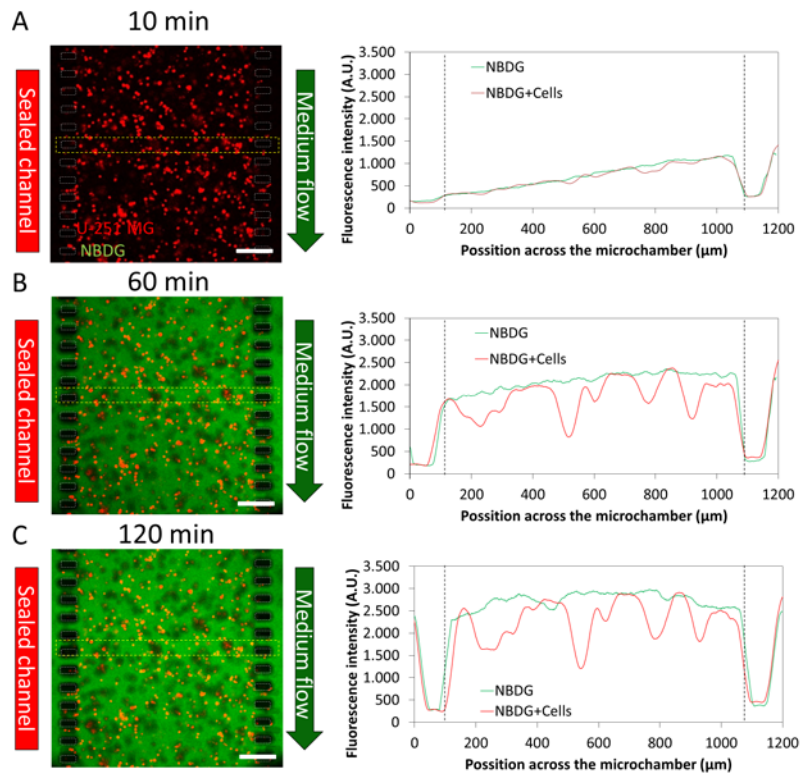

710

711

712 **Supporting Fig 2.**
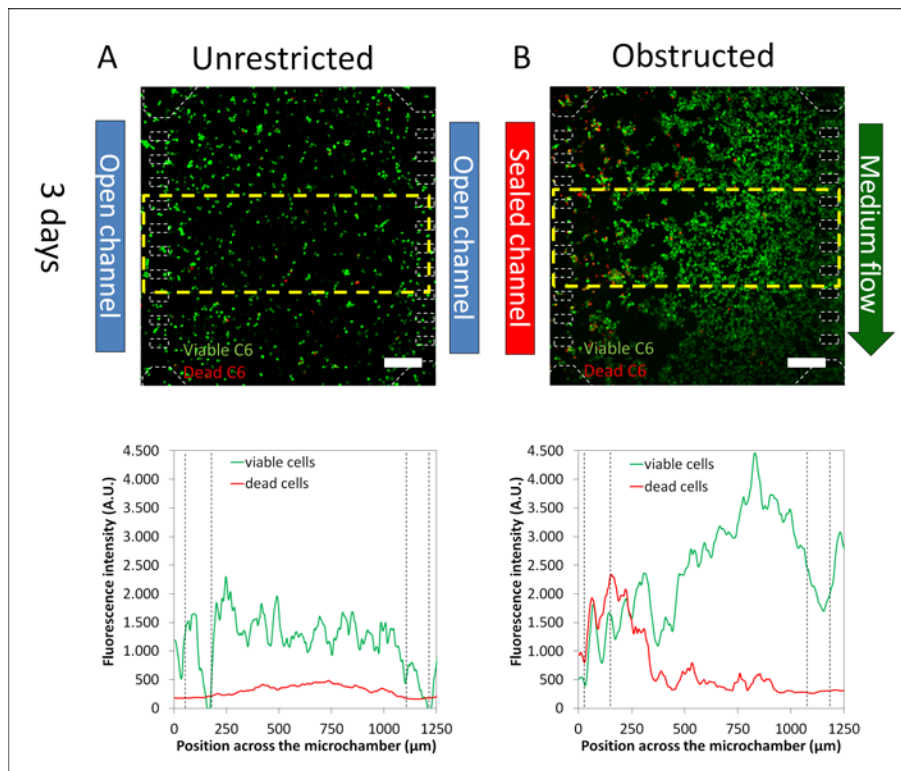
713

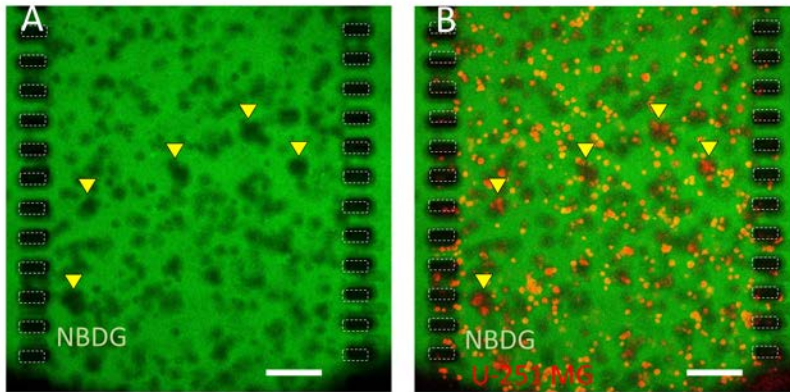714

715   **Supporting Fig 3.**

716

717

718
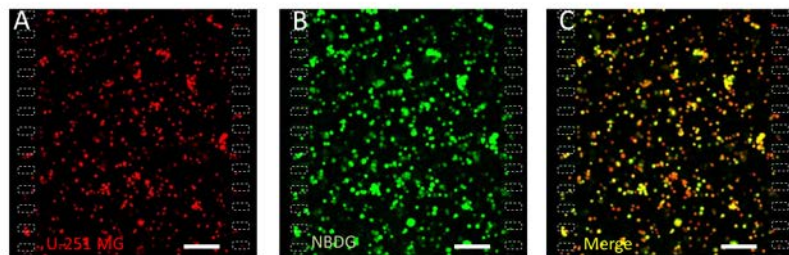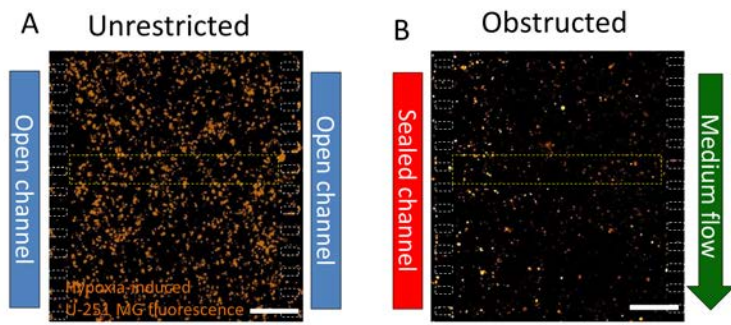
719 **Supporting Fig 4.**

720

721

722   **Supporting Fig 5.**

723

724

725

726   **Supporting Fig 6.**

A   Unrestricted   B   Obstructed

Open channel | Open channel | Sealed channel | Medium flow

Hypoxia-induced U-251 MG fluorescence

727